Aerofoil-Vortex Interaction Simulation Using the Compressible Vorticity Confinement Method

R. Morvant[*] K.J. Badcock[†] G.N. Barakos[‡] B.E. Richards[§]
CFD Laboratory
Department of Aerospace Engineering
University of Glasgow, Glasgow G128QQ, UK

The phenomenon of Blade-Vortex Interaction (BVI) is central to the study of the aerodynamics of rotors as well as to the calculation of the acoustic field radiated by rotorcraft. The simulation of BVI is challenging since the solution scheme tends to alter the characteristics of the vortex which must be preserved until the interaction. The Compressible Vorticity Confinement Method (CVCM) is capable of preserving vortical flows without major modifications to existing CFD codes. Inviscid and viscous calculations have been carried out for a well-know head-on BVI case. The results obtained using the CVCM show a good agreement with the measurements.

Nomenclature

ε	Confinement parameter
$\hat{\Gamma}$	Normalised circulation
μ	Numerical viscosity
ω	Vorticity
ρ	Density
$\vec{f}_b$	Body force term
$\vec{n}$	Normalised vorticity gradient vector to the surface S
$\vec{V}$	Velocity vector
BVI	Blade Vortex Interaction
$CVCM$	Compressible Vorticity Confinement Method
NS	Navier-Stokes
r	Distance from the vortex core
R_c	Viscous core radius
SPL	Sound Pressure Level
C_p	Surface pressure coefficient

[*] Research student
[†] Reader
[‡] Lecturer
[§] Professor

1 Introduction

BVI noise should be considered when simulating the acoustics of a helicopter due to its high contribution to the perceived noise levels. BVI takes place both on the main and tail rotors of helicopters with the vortex axis being parallel or orthogonal to the blades. The BVI noise is generated when the blade tip vortices collide or come close to the rotor blades [1]. As explained by Schmitz et al [2], the unsteady disturbances generated by the passage of a vortex close to a blade radiate a part of their energy as sound. Depending on the phase delay between the emitted acoustic waves, the BVI sound may propagate directionally and far from the rotor. It is therefore essential to understand the mechanisms of BVI due to its dominance on the acoustic signature of a helicopter, particularly in descending flight [3, 4].

In recent years, Computational Fluid Dynamics (CFD) has made a significant impact in the design of modern rotors. Yet, the ability of most CFD codes to preserve vortices over long periods of calculation on grids of moderate density still remains questionable. This is mainly due to the amount of numerical dissipation and dispersion inherent in most numerical schemes. The PMB code of the University of Glasgow [5] is the basis of the present work. This is a parallel, structured, multi-block code with implicit time stepping. It is based on Osher and Roe schemes and uses a preconditioned

Krylov solver for high efficiency.

To extend the capability of the code for predicting flows with strong vortical structures the Compressible Vorticity Confinement Method (CVCM) [6, 7, 8] has been implemented. This method is particularly attractive from a practical point of view since it is economic in terms of memory and CPU time and relatively simple to implement in existing CFD solvers. This method has been successfully used for tracking vortices [9, 10] and more specifically for rotorcraft simulations [11]. Application of the method is also reported for several other flow cases including flows over complex bodies [12], massively separated flows [13] and even flow visualization [14]. Recently, it was applied to allow the simulation of blade-vortex interaction [6] which is the main focus of this paper.

The well-know experiment of Lee and Bershader [15] provides the basis of the current work. This experiment concerns the head-on parallel BVI between a vortex and a NACA0012 aerofoil. Since detailed measurements of the surface pressure on the upper and lower sides of the blade are available for this experiment, this popular case has been previously used for evaluating simulations. Different techniques such as high-order schemes [15, 16], local grid refinement [17] and more recently unstructured adaptive meshes [18, 19] were used to preserve the convected vortex. CVCM allows the use of relatively coarse grids along the vortex path and refined grids near the aerofoil so that accurate predictions of the surface pressure and well-preserved near- and mid-field acoustical waves can be obtained.

The complex flow-field of the head-on BVI is known to produce a very intense impulsive noise [15]. As mentioned in [6] [20], this noise has four main contributions (i) from the vortex at subsonic speed with its upwash or downwash velocity component, (ii) from the stall and reattachment of the flow when the vortex approaches the aerofoil, (iii) from the oscillation of the stagnation point due to the high pressure region generated at the leading-edge and (iv) of the aerofoil (compressibility waves) and (iv) from the development of a supersonic area at the shoulder of the aerofoil (transonic waves).

This paper will first illustrate the capabilities of the Vorticity Confinement Method using the simple benchmark problem of vortex convection in an infinite domain. Once confidence in the method is established the simulation of the head-on BVI will be attempted along with comparisons between CFD results and the experiments of Lee and Bershader [15]. Parameters which are likely to influence the BVI results will be studied: vortex location, spatial and time refinement and the influence of corrections to the angle of attack. Finally, the nearfield acoustics of the NACA0012 will be presented along with Mach number effects.

2 The Compressible Vorticity Confinement Method

2.1 Principles of the VCM

The Vorticity Confinement Method (VCM) developed by Steinhoff [7] is aimed at countering the dissipation of the scheme. The VCM is based on the observation that the scheme tends to dissipate the vortices in the flow. Therefore the VCM adds a source of momentum in regions of the flowfield where vorticity is concentrated to balance this. The basic modification is to add a body force term $\vec{\mathbf{f_b}}$ to the momentum transport equations which for incompressible flow reads

$$\rho\frac{\partial\vec{\mathbf{V}}}{\partial t}+\rho(\vec{\mathbf{V}}.\nabla)\vec{\mathbf{V}}+\nabla p=\mu\nabla^2\vec{\mathbf{V}}-\vec{\mathbf{f_b}}$$

The body force term $\vec{\mathbf{f_b}}$ is given by $-\rho\varepsilon\frac{|\Delta\vec{\omega}|}{|\Delta|\vec{\omega}||}\times\vec{\omega}$ where ε, μ and $\vec{\omega}$ are respectively the confinement parameter, an artificial viscosity term and the vorticity.

2.2 Compressibility modifications

The extension of the VCM to the compressible Navier-Stokes (NS) equations has been realised by including the work of the body source term in the energy equation [21]. The integral form of the NS equations can be rewritten for a two-dimensional problem as

$$\frac{d}{dt}\int_\vartheta W d\vartheta+\int_\Sigma F.\vec{\mathbf{n}}d\Sigma+\int_\Sigma G.\vec{\mathbf{n}}d\Sigma=-\int_\vartheta S d\vartheta$$

where the conservative variables W, the fluxes F, G and the source term S can be expressed as

$$W=\begin{Bmatrix}\rho\\ \rho u\\ \rho v\\ \rho e\end{Bmatrix},F=\begin{Bmatrix}\rho u\\ \rho u^2+p\\ \rho uv\\ \rho uh\end{Bmatrix},G=\begin{Bmatrix}\rho v\\ \rho uv\\ \rho v^2+p\\ \rho vh\end{Bmatrix},$$

$$S=\begin{Bmatrix}0\\ \varepsilon\rho\,(\vec{\mathbf{n}}\times\vec{\omega}).\vec{\mathbf{i}}\\ \varepsilon\rho\,(\vec{\mathbf{n}}\times\vec{\omega}).\vec{\mathbf{j}}\\ \varepsilon\rho\,(\vec{\mathbf{n}}\times\vec{\omega}).\vec{\mathbf{V}}\end{Bmatrix}\ with\ \begin{cases}\vec{\mathbf{n}}=\frac{|\nabla\vec{\omega}|}{|\nabla|\vec{\omega}||}\\ \vec{\omega}=\frac{\partial}{\partial\mathbf{M}}\times\vec{\mathbf{V}}\end{cases}$$

The term $-\rho\varepsilon\frac{|\Delta\omega|}{|\Delta|\omega||}\times\omega$ is added to the transport equations of the momentum components, while ε, ρ and ω represent the confinement parameter, the density and the vorticity, respectively. In order to include the work

done by the body source term in the energy conservation law, the term $-\varepsilon\rho(\vec{\mathbf{n}}\times\vec{\omega})$ also contributes as a part of the residual. Note that a complete review of the Compressible Vorticity Confinement Method is given in the thesis by Yu [22].

2.3 Implementation

The vorticity gradient is required for the source term S. The derivatives were calculated from their curvilinear form. It was found that the performance of the method depends strongly on the order of accuracy of the calculated gradients. Therefore the derivatives f_i' were estimated using the fourth-order finite difference approximation as follows

$$f_i' = \frac{-f_{i+2}+8f_{i+1}-8f_{i-1}+f_{i-2}}{12}$$

The use of high-order derivatives provides a better estimation of the vorticity gradients particularly in the wake of the aerofoil. In addition, some Laplacian smoothing to the vorticity and its gradient was also applied to get smoother source terms. Regarding the temporal treatment, the Jacobians in the implicit formulation were left unchanged. Experience with the test cases presented in this paper (see section 4.2.3) has shown that the stability and convergence of the scheme is very similar for different time refinements.

2.4 Modifications to the basic method

Different methods have been used to set the values for the parameters ε and μ.

(a) Parameters ε and μ set to constants.
The constant ε and μ were respectively chosen so as to control the amount of momentum injected into the flow and to remove any excessive momentum which may create artificial vortices. The value of ε ranges typically from 0.001 to 0.1 whereas the parameter μ was set to a value from 0.1 to 0.

(b) Use of a vorticity gradient based limiter.
It has been attempted to reduce the production of spurious vortices via the use of a limiter based on the vorticity gradient. Indeed, it was observed that some of the secondary vortices stem from the vector $\vec{\mathbf{n}}$. The cross product of the vector $\vec{\mathbf{n}}$ and the vorticity $\vec{\mathbf{w}}$ allows the concentration of the anti-dissipation term in the areas given by the vector $\vec{\mathbf{n}}$, the normalised ratio of the vorticity gradient amplitude. However, the ratio may have a large value even for areas of low vorticity, implying that artificial vortices may be created in zones where the value $|\vec{\mathbf{n}}|$ is large. Therefore, $\vec{\mathbf{n}}$ was set to zero when the magnitude of the vorticity gradient $|\Delta|\vec{\omega}||$ was low.

(c) Parameter ε scaled with the grid.
Different formulations of the CVCM have also been tested by other authors [9, 23, 24]. Since the confinement parameter ε is homogeneous to a velocity, it is possible to scale it with the grid size. The formulation proposed by Yu [24] expresses the confinement parameter as $\varepsilon = h^2|\nabla|w||$ with h the characteristic length which is equal to the scalar product of the cell size vector $\vec{\mathbf{L}} = (\Delta x, \Delta y, \Delta z)$ with the vector $\vec{\mathbf{n}}$. This formulation has been tested and compared against the constant scaling ε. Results are shown in section 3.

3 Evaluation of the CVCM on a vortex convection test

The CVCM has been tested on the benchmark problem of vortex convection in an infinite domain. An isentropic vortex is introduced into the flow and convected at the free-stream velocity. Periodic boundary conditions were applied to enable the vortex to convect for many cycles. The Sculley model was chosen due to its wide acceptance in the literature [15]. According to this model, the expression for the tangential velocity component is as follows:

$$\frac{v_\theta}{V_\infty} = \frac{\hat{\Gamma}}{2\pi r}\frac{r^2}{r^2+R_c^2}$$

with V_∞, $\hat{\Gamma}$, a_o being respectively the freestream velocity, the non-dimensionalised circulation ($\hat{\Gamma} = \frac{\Gamma}{V_\infty L}$) and the core radius. Note that the pressure and density are calculated from the approximation of the Euler equations $\frac{dp}{dr} = \rho\frac{u_\theta^2}{r}$ and the isentropic relation $p = c\rho^\gamma$ [22].

The influence of the confinement parameter and of the viscosity term is examined for the case $R_c = 0.018$, $\hat{\Gamma} = -0.283$, $M = 0.5$. The calculations were carried out on two uniform grids: a coarse grid with 51×102 and a finer grid of 913×278. Different values for the confinement coefficient ε have been used, the viscosity term being set to zero. The flow was first considered as laminar with a Reynolds number of 1000. The initial condition and the vorticity divided by the density are plotted in Figure 1. Figure 1(a) highlights the grid density of the coarse grid. Note that the full grid extends from -5 to 5 in the X direction and from -1.0 to 1.0 in the Y direction. Figure 1(b) shows that the ω/ρ ratio is maintained constant when the CVCM is used while it is significantly reduced when $\varepsilon = 0$.

It was also noticed that the method leads to the formation of artificial secondary vortices when the dissipation term is set to zero (Figure 2(a)). As depicted in Figure 2, the dissipation term (method (a)) reduces the creation of artificial vortices and results in better preservation of the shape of the original vortex.

Results with the use of the vorticity gradient based limiter (method (b)) are presented in Figure 2(b). The shape of the vortex is better preserved even when the artificial viscosity is set to zero and all secondary vortices have now disappeared. The gradient based limiter was used to replace the dissipation term so that only the confinement term ε remains as a parameter of the CVCM. Comparison between the results given by method (c) and method (b) with the use of the limiter shows that the vortex is better convected when the characteristic length is used. This is depicted in Figure 3 where results are shown after 02 cycles of vortex convection. It can be noticed (Figure 3(a)) that the vortex is better captured on a fine grid than on a coarse grid since the number of cells across the core radius is larger.

The use of the CVCM allows the tracking of the vortex for several cycles. As illustrated in Figure 3(a), on the coarse grid, the vortex is well-preserved even after twenty cycles whereas it disappears after only two cycles without CVCM. On the fine grid and without CVCM, the vortex is five times weaker in terms of the ω/ρ ratio at the vortex core after twenty cycles of convection (see Figure 3(b)). The combination of methods (b) and (c) gives the best results for preserving the vortex characteristics and was therefore preferred to method (a). Note that the CPU time incurred by the use of the CVCM is minimal.

4 Optimisation of the BVI Simulations using the CVCM

Next an aerofoil test case is considered to determine the capabilities of the CVCM and to find the best options for simulating BVI. The test case here is the parallel BVI between a clockwise vortex and a NACA 0012 aerofoil. The radius of the vortex and its circulation are set respectively to 0 018 and 0 - 283 as for the benchmark problem. A schematic is presented in Figure 4. Both inviscid and viscous calculations were carried out. Results will be shown for the head-on BVI at freestream Mach numbers of 5 and 0 of 8.

4.1 Characteristics and behaviour of the CVCM for the BVI simulation

The simulation of BVI requires the use of non-uniform grids. The scaling with the cell size was therefore combined with the vorticity gradient limiter for the BVI study. The grid used for the BVI simulation was carefully generated so that spacing along the expected path of the vortex is as uniform as possible. Moreover, the CVCM was not needed near the aerofoil since the grid was fine enough in this area to capture the vortices. In addition, some robustness problems occurred when running the calculations for values of ε which are too large. Indeed, the use of the CVCM tends to modify the profile of the boundary layer and to amplify the wake which is characterised by a large value of vorticity. Therefore, zones are used to restrict the effect of the source term to vortices avoiding wakes and boundary layers the confinement method was not applied until a distance 01 chords from the aerofoil and also when the vorticity gradient exceeded fi value o No confinement was applied near the aerofoil so that the CVCM does not alter the behaviour of the turbulence model during the interaction. Note that the optimum ε parameter was found to depend on the used spatial schemes of which dissipation properties vary with the grid cell length, the time step and the nature of the flow. The parameter ε was estimated to 1.5 for the subsonic case and to 1.8 for the transonic case (see section 4.2).

4.2 CFD Calculations

The importance of different parameters has been evaluated vortex l ocation, spatial and time refinement and angle of attack. Inviscid and viscous calculations have been attempted and the Reynolds number was set to one million for the viscous case. This corresponds to the range of values 0.9×10^6-1.3×10^6 given by the experiments. The viscous calculations were expected to predict better the pressure coefficient on the lower part of the aerofoil. As will be shown, it is essential to include the viscosity effects since they a the transfer of energy between vortices as well as between a vortex and the boundary-layer flow as mentioned by Körber and Ballmann in [25]. The best parameters for simulating BVI will be determined by examining the results obtained for the low-speed case (freestream Mach number 0 5). Then the results for a similar head-on BVI at a freestream Mach number of 8 will be presented.

4.2.1 Influence of the vortex location

The vortex location is of great importance since the vortex model needs to be introduced in a potential-

like flow region. Different locations have been tested to check whether the history of the pressure coefficient changes and whether the vortex is preserved in a similar way for different initial locations. Four locations have been used namely 1.5, 2.5, 3.5 and 4.5 chords ahead of the aerofoil. Fine and coarse versions of inviscid and viscous grids were generated. The difference between the grids is only in the spacing used around the aerofoil. Figure 5 presents the comparison between the experiments and predictions, on a fine grid of approximately 500k points , for the surface pressure history. The results using the CVCM compare very well against the experiments for the four vortex locations. The pressure coefficients are well predicted whereas they are very much underestimated when no CVCM is applied. The vortex location does not seem to affect the prediction of pressure coefficient assuming the optimum confinement parameter ε is used.

The k-ω model was used for viscous calculations. First, as for the inviscid calculations, the trace of the interaction on the Cp is very weak when no confinement is used. Secondly the viscous results are in very good agreement with the experiments. Better agreement against the experiments is obtained for viscous calculations especially for the pressure coefficient at the lower surface (see Figure 6). This is expected as viscosity makes the encounter less impulsive [26]. In fact, viscous calculations can reasonably predict the oscillation of stagnation point [27] and flow separation [17] which determines the movement of the high-pressure region towards the low-pressure region near the left of the aerofoil (see Figure 12) [15]. As explained in [17, 27, 28], a secondary vortex is formed beneath the aerofoil due to the flow separation. The induced velocity of the clockwise-rotating vortex makes the stagnation point move up. Then the flow speed decreases on the upper surface and increases on the lower surface leading to the creation of a secondary anti-clockwise vortex. The original and the secondary vortices get weakened after combining and they separate more and more from the aerofoil. This explains why their effects on the flow over the aft of the aerofoil is minimal. The density contours are compared against the experiments in Figure 7 and good agreement is obtained.

4.2.2 Influence of the spatial refinement

Two grids of different density along the vortex path have been used for the inviscid runs: a coarse grid of 125k points and a fine grid of 485k points. The coarse and fine grids have respectively around 2 and 4 cells across the core radius, corresponding to a similar grid density as in the benchmark problem (see Figure 1(a)). The ε parameters for the coarse and fine grids were respectively set to 1.5 and 0.75. Again, the Cp is well predicted on both grids (see Figure 8). It was found that the good agreement depends on the choice of the ε parameter. The value of ε was chosen according to the cell area along the vortex path for a given grid. Knowing the optimum ε value for a particular grid density, it is possible to estimate the ε value on another uniform grid by simply assuming it is inversely proportional to the cell area.

Viscous calculations were run on two grids for the k-ω model: a coarse grid of 1022 points and a fine grid of 8200k points. Results are similar on both grids for the main interaction as shown in Figure 9. However, some oscillations occur after the main interaction on the fine grid. This is apparently due to the scaling used for the ε parameter.

4.2.3 Influence of the time refinement

The vortex was introduced at 1.5 chords ahead of the aerofoil and calculations were carried out on the coarse grid of 125k points. As depicted in Figure 10, the Cp values are very well predicted for the different time steps. Differences appear at the chordwise section $x/c=0.05$, that is unlikely to affect the acoustical pressure since the main interaction near the LE is well predicted. The use of a small time step is advisable only if secondary vortices in the flow are to be captured (see below).

Viscous calculations were run using the k-ω and SST models for two different time steps: 0.01 and 0.001 with the vortex being introduced at 2.5 chords ahead of the aerofoil. The time refinement was found to modify the strength of the secondary vortex as the Cp value at $x/c=0.05$ as for the inviscid calculations, the k-ω model being more sensitive to the time refinement. The main acoustical wave is captured in a similar way for both models, that seems to indicate that a time of 0.01 is sufficient to get an estimation of the SPL for this test case.

4.2.4 Influence of the angles of attack

It is noticeable that the computed Cp pressure does not match the experiments before the interaction as if an angle of attack was present. It was suggested [26] that the clockwise-rotating vortices decrease locally the apparent angle of attack when passing below the aerofoil, i.e. they unload the blade. Therefore two viscous calculations with angles of attack 0.5 and 0.75 degrees were carried out. The k-ω model was used and the vortex was introduced at 2.5 chords ahead of the aerofoil. Not only the presence of a small angle of attack gives a better match against the experiments regarding the Cp

history before the interaction, but it also gives weaker Cp values at sections $x/c=0.05$ and $x/c=0.10$, as illustrated by Figure 11.

Regarding the Cp values for $x/c=0.02$, the interaction appears stronger for zero angle of attack due to the vortex path. After the vortex break-up, a larger part of the vortex propagates on the lower side of the aerofoil (see Figure 12), explaining why the anti-clockwise rotating secondary vortex is stronger in the case of zero angle of attack. Then the interaction weakens as the secondary vortex mixes with the original one.

4.2.5 Transonic case

Results are now discussed for a transonic flow of a freestream Mach number of 0.8. The history of the pressure coefficients is shown in Figure 13. Despite the fact that the most pronounced interaction is observed when the vortex passes under the aerofoil, at transonic flow, the magnitude of the peaks for the loads are weaker. This may stem from the presence of shocks. The vortex while moving at the surface of the aerofoil encounters the shock, thickens the shock and regains some strength, that explains why the Cp bandwidth is larger. Regarding the history of the lift, it is interesting to establish a comparison between the subsonic and transonic flows (see Figure 14(a)). As mentioned in [30], the lift coefficient is observed to be positive when the vortex induces a downwash at the L.E. of the aerofoil at both subsonic and transonic flows. Afterwards, when the vortex passes the T.E., the lift coefficient rapidly increases. The lift for the transonic flow is less affected by the passage of the vortex which is now weakened by the presence of the shock. For the transonic case, the same vortex properties as for the subsonic one have been used, unfortunately no BVI experiments are available for higher Mach numbers. Figure 14(b) presents the time history of the density at the vortex core for both Mach numbers used in this work.

5 Aerofoil-Vortex Noise Simulation

So far the aerodynamics of the interaction, as characterised by the surface pressures, have been considered. The difference considering acoustics makes is now discussed. The first parameter to be checked for the calculations of the acoustical pressure was the vortex location. Although the pressure coefficient can be correctly predicted for the four different vortex locations (see section 4.2.1), non physical waves appear. Indeed, at the first time steps, the difficulties of the solver for perfectly assimilating the vortex into the flow solution is manifested by the creation of spurious waves that start to propagate from the aerofoil. An acoustical analysis is spoiled by the presence of these waves and necessitates the vortex to be introduced at least 4.5 chords ahead.

The same head-on BVI has been simulated for the NACA0012 for subsonic and transonic flow conditions. The Cp history and the acoustical pressure of the vortex-aerofoil interaction are presented in the next sections. It will be shown that the BVI noise is determined by three mechanisms of aerodynamic sound generation: the compressibility waves, the transonic waves [20, 25] and the trailing-edge noise [6].

5.1 High subsonic flow

The high directivity of BVI noise is usually illustrated by two distinct radiation lobes. These two waves are called compressible waves which are typical for high subsonic flow at the vortex break-up [31, 32]. The presence of the vortex causes the unsteady displacement of the stagnation point of the flow at the L.E. of the aerofoil. Then an enlarged high-pressure region is generated and then propagates upstream like steepening shock waves [33]. The two waves which are denoted by A and B in Figure 15(a) are generated below and above the aerofoil. Once these waves have reached the trailing-edge, other waves start to form and propagate upstream resulting in trailing-edge noise. The trailing-edge waves are depicted by C and D.

Placing a probe at point P (see Figure 15(a)), and plotting the trace of SPL, one can see the passage of the acoustic wave A. The effect of this wave on the SPL is the peak shown in Figure 15(b) at time $tU_\infty/c=5.00$.

5.2 Transonic flow

An additional acoustical wave apart from the compressibility and the trailing-edge ones is present for transonic flow. This wave called the transonic wave emerges when a supersonic flow region is generated along the shoulder of the aerofoil [33]. As explained in [20, 25], a shock wave appears after the vortex reaches the maximum thickness of the aerofoil beyond which the supersonic area collapses. Then the shock wave moves upstream leaving the T.E. in a downward direction while the stagnation point moves upwards. This results in the generation of a sound wave propagating upstream [32]. The acoustical pressure and the Mach number contours for two instances are given in Figures 16 and 17 with the acoustical wave denoted by A. As expected, the compressible and trailing-edge wave are also present

for the transonic flow case (see Figure 17). It has to be noticed that there are significant differences in the strength and direction of the acoustical waves between the two Mach numbers. Despite the fact that the passage of the vortex does not perturb as much the loads of the aerofoil in the transonic case, the level of acoustical pressure are higher than those for the subsonic case. The directivity patterns of the noise are different due to the presence of the shocks which modify the trajectory of the acoustical waves. It is also interesting to note that it takes more time for the acoustical waves to be generated for the transonic case than for the subsonic one (see Figure 15(b)).

6 Conclusion

Present results indicate that accurate predictions of BVI can be obtained using the CVCM. The accuracy of the predictions is good given the complexity of the problem and first indications reveal that the predictions are not so sensitive to the parameters of the method considering that different grids with the appropriate epsilon give similar results. The CVCM made possible the simulation of BVI using an existing CFD code and the overhead in terms of CPU time and memory was minimal. Further investigation is needed to make the method as independent as possible from the value of the confinement parameter, that could be possibly achieved by taking into account the properties of the scheme of the solver.

The present calculations demonstrate that accurate prediction of the surface pressure coefficient is possible for head-on BVI cases. The predicted acoustic field is in qualitative agreement with experimental observations. However, additional validation cases are necessary to improve the fidelity of the CFD results. Direct comparison between acoustic measurements and CFD would be beneficial and this could reveal further limitations stemming from the order of the employed numerical scheme.

Acknowledgements

This work was supported by Westl and Helicopter Limited.

References

[1] ER. Boxtel. Experimental observations of two-dimensional blade-vortex interaction. *AIAA Journal - Vol.28, No. 8, pp 1353-1359*, August 1990.

[2] H. Schmitz et al. Flight path management and control methodology to reduce helicopter blade-vortex interaction (bvi) noise. *Journal of the American Helicopter Society*, 2000.

[3] J W. Leverton. 25 years of rotorcraft aeroacoutics: Historical perspective and important issue. *Journal of Sound and Vibration 123(2), pp.62-287*, 1989.

[4] F.X. Caradonna and H C. Tung. Helicopter impulsive noise: Theoretical and experimental status. *Journal of Sound and Vibration 109(3), pp.63-422*, 1986.

[5] K J. Badcock and B. Richards. Implicit time-stepping methods for the Navier-Stokes equations. *AIAA. Vol. 34, No. 3*, March 1996.

[6] J Steinhoff and K.G Raviprakash. Navier-Stokes computation of blade-vortex interaction using vorticity confinement. *AIAA paper 95-0161*, 1995.

[7] J Steinhoff et al. The computation of flow over helicopter rotors and complex bodies using vorticity confinement. Technical report, TN 37388, University of Space Institute, Tullahoma, USA, 2001.

[8] J Steinhoff and D. Underhill. Modification of the Euler equations for vorticity confinement: Application to the computation of interacting vortex rings. *Journal of Physics Fluid 6 (8), August*, 1994.

[9] R. Lonher and C. Yang. Tracking vortices over large distances using vorticity confinement. *ECCOMAS CFD 2001, Swansea, Wales, Sept*, 2001.

[10] M. Murayama, K. Nakahashi, and S. Obayashi. Numerical simulation of vortical flows using vorticity confinement coupled with unstructured grid. *AIAA paper 2001-0606*, 2001.

[11] Wenren et al. Efficient eulerian computation of realistic rotorcraft flows using vorticity confinement. *AIAA-2001-0996, 39th AIAA Aerospace Sciences Meeting and Exhibit 8-11 Jan*, 2001.

[12] W Dietz et al. Application of vorticity confinement to the prediction of the flow over complex bodies. *AIAA-2001-2642 CFD Conference 11-14 June*, 2001.

[13] Gu and B. Grossman. The computation of massively separated flows using compressible vorticity confinement methods. *AIAA paper 2002-1365 4*, 2002.

[14] R. Fedkiw et al. Visual simulation of smoke. *to appear in the SIGGRAPH conference proceedings*, 2000.

[15] S. Lee and D. Bershader. Head-on parallel blade-vortex interaction. *AIAA Journal Vol. 32, No. 1*, January 1994.

[16] S. Lee and D. Bershader. An experimental and computational study of 2-d parallel blade-vortex interaction. *AIAA paper91-3277*, September 1991.

[17] N. Ng and H.R. Vier. Numerical investigation of the transonic blade-vortex interaction. *AIAA paper 97-1846*, June 1997.

[18] W.S. Oh, J.S. Kim, and O.J. Kwon. An unstructured dynamic mesh procedure for 2-d unsteady viscous flow simulations. *AIAA paper 2002-0121*, January 2002.

[19] W.S. Oh, J.S. Kim, and O.J. Kwon. Numerical simulation of two-dimensional blade-vortex interactions using unstructured adaptive meshes. *AIAA Journal Vol. 40, No. 3*, March 2002.

[20] H.-M. Lent et al. Mechanisms of transonic blade-vortex interaction noise. *Journal of Aircraft, Vol. 30 No 1, Jan.-Feb.*, 1993.

[21] G. Hu and B. Grossman. Numerical method for vorticity confinement in compressible flow. *AIAA Journal, Nov. 1*, October 2002.

[22] G. Hu. *The Development and Applications of a Numerical Method for Compressible Vorticity Confinement in Vortex-Dominant Flows* PhD thesis, Viginia Polytechnic Institute and State University, Blacksburg, Virginia, June 2001.

[23] M. Costes and G. Iwani. An automatic anti-diffusion method for vortical flows based on vorticity confinement. *Aerospace Science and Technology, 7*, pp. 11-21, 2003.

[24] M. Fan, Y. Wereley, W. Dietz, M. Xiao, and J. Steinhoff. Computing blunt body flows on coarse grids using vorticity confinement. *Journal of Fluids Engineering - Vol. 124, pp. 876-885*, December 2002.

[25] S. Körber and J. Ballmann. Mechanisms and acoustics of blade-vortex-interactions. *Flugwiss. Weltraumforsch. 19, pp. 39-406 - Springer-Verlag*, 1995.

[26] J.C. Hardin and S.L. Lamkin. Aeroacoustic interaction of a distributed vortex with a lifting Joukowski airfoil. *AIAA paper 84-2287*, October 1984.

[27] C. Tung, H. Yu, and Y. Yu. Aerodynamic aspects of blade-vortex interaction (bvi). *AIAA paper 96-2010*, June 1996.

[28] M. Mandella and D. Bershader. Qualitative study of the compressible vortex: Generation, structure and interaction with airfoils. *AIAA paper 87-0328*, January 1987.

[29] M.C. Wilder and D.P. Telionis. Parallel blade-vortex interaction. *Journal of Fluids and Structure - 12, pp. 818-838*, 1998.

[30] M.M. Rai. Navier-Stokes simulations of blade-vortex interaction using high-order accurate upwind schemes. *AIAA paper 87-0543*, January 1987.

[31] H.Y. Yu. Rotor blade-vortex interaction noise. *Progress in Aerospace Sciences 33 97-115*, 2000.

[32] W.S. Kaminski and A.P. Szumowski. Acoustic effects of parallel vortex-airfoil interaction. *Journal of Sound and Vibration - 183(2), 209-220*, 1995.

[33] J.L. Elzey and H.M. Reeke. The acoustic wave from a shock-vortex interaction: Comparison between theory and computation. *Fluid Dynamics Research 27, pp. 53-64*, 2000.

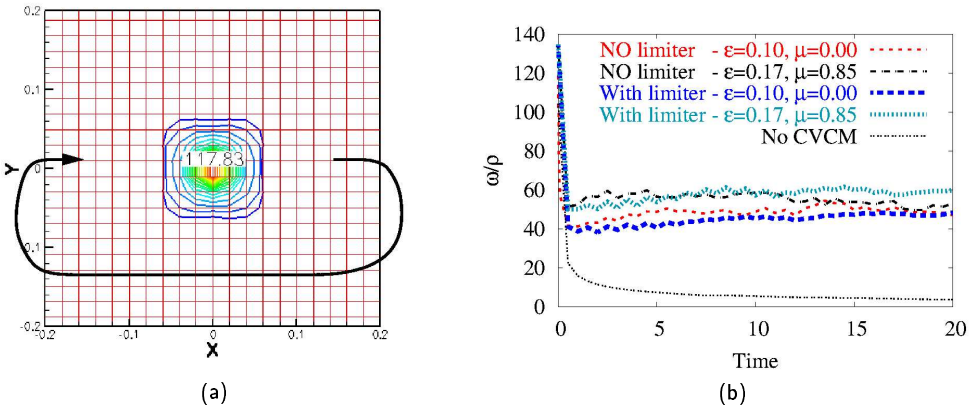

(a) (b)

Figure 1: (a) Schematic of the initial conditions of the benchmark problem and (b) time history of the ω/ρ ratio at the vortex core as predicted using the CVCM method with or without gradient-based vorticity limiters.

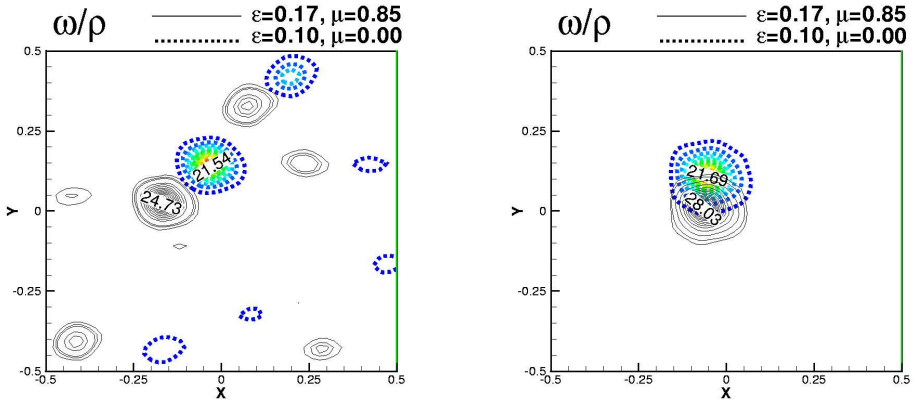

(a) No limiter (b) With limiter

Figure 2: Contours of the ω/ρ ratio after 2 cycles: (a) Effects of the numerical viscosity (μ) and (b) effect of the gradient-based vorticity limiter on the coarse grid.

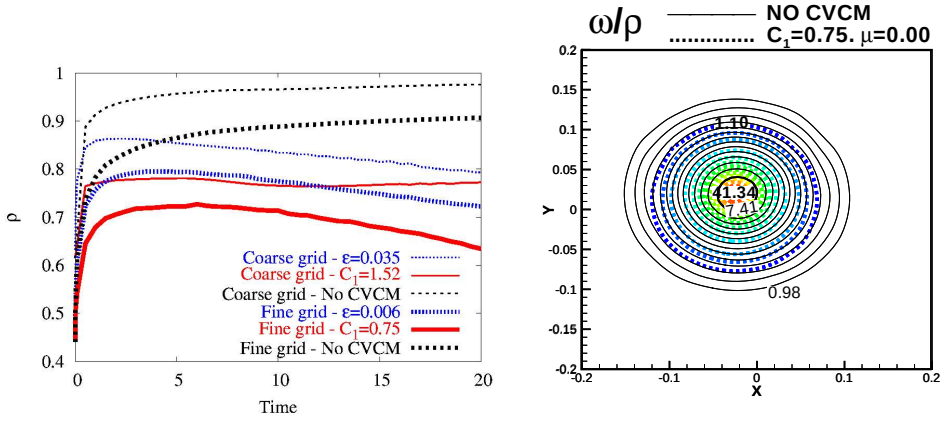

(a) (b)

Figure 3: (a) Time history of the density at the vortex core using different ε scalings. (b) Evolution of the ω/ρ ratio after 2 cycles with and without CVCM.

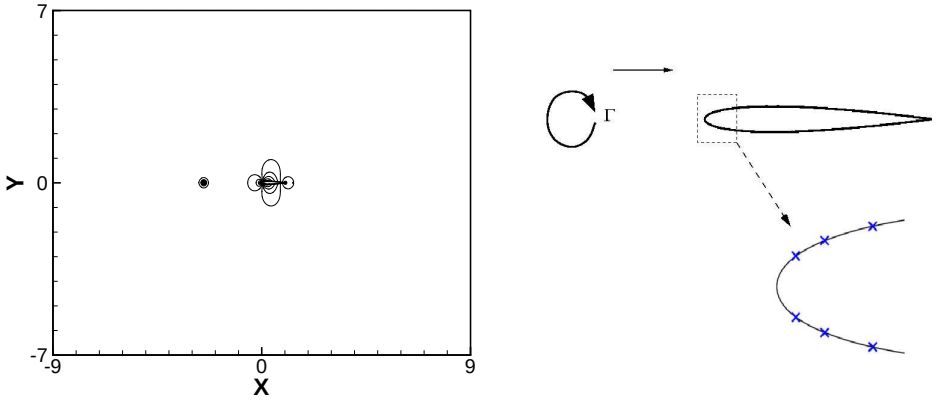

(a) (b)

Figure 4: (a) Schematic of the initial configuration of the head-on BVI problem, the initial location of the vortex is shown along with pressure contours. (b) Locations of the pressure taps in the leading-edge region of the aerofoil. The locations correspond to the experiments by Lee and Bershader [15].

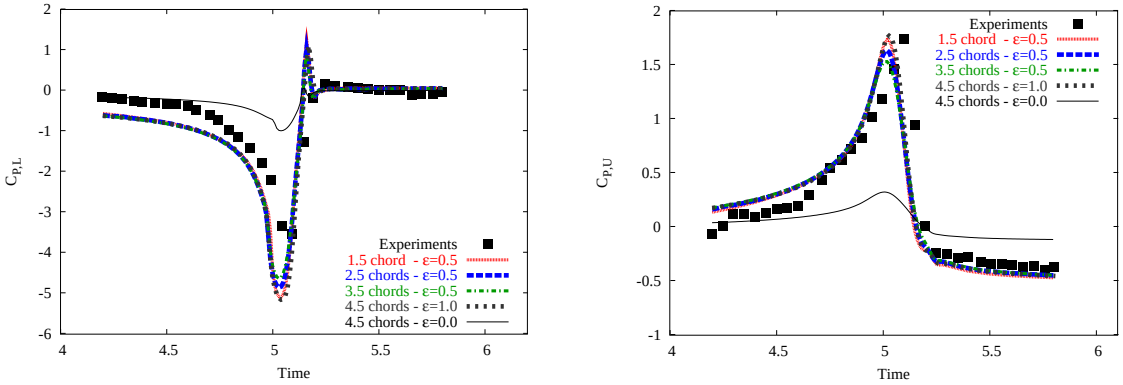

(a) Lower surface, x/c=0.02 (b) Upper surface, x/c=0.02

Figure 5: Influence of the initial vortex location on the time history of the surface pressure coefficient. Head-on BVI problem, NACA0012 aerofoil, inviscid calculation, Mach number 0.5, x/c=0.02.

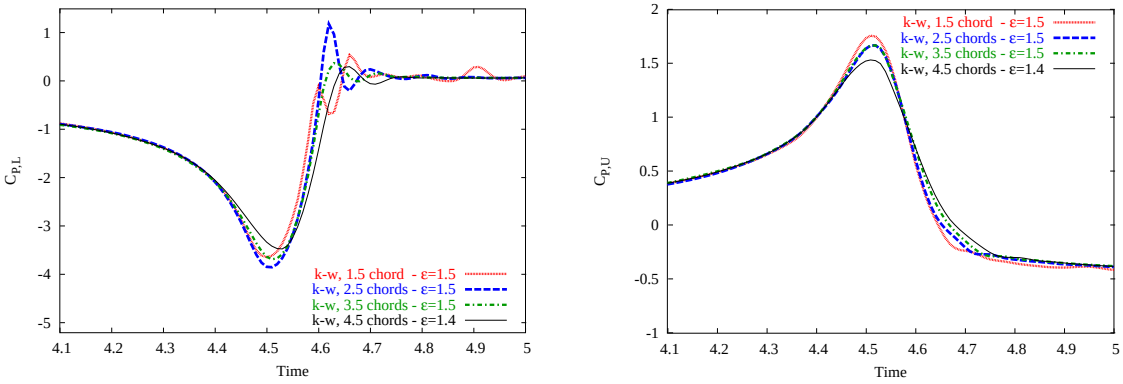

(a) Lower surface, x/c=0.02 (b) Upper surface, x/c=0.02

Figure 6: Influence of the initial vortex location on the time history of the surface pressure coefficient. Head-on BVI problem, NACA0012 aerofoil, viscous calculation, Mach number 0.5, x/c=0.02.

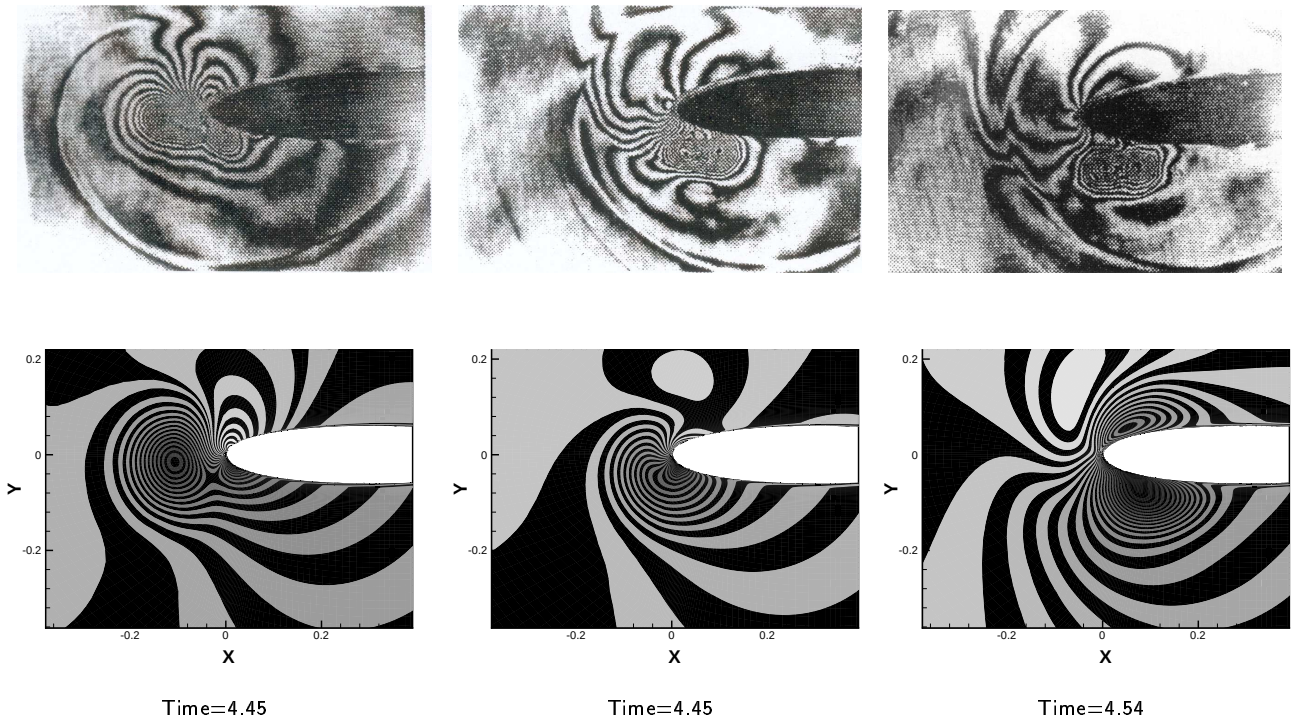

Figure 7: Comparison between experimental holographic interferograms and computational density contours for the head-on BVI case. The vortex was introduced 4.5 chords ahead of the aerofoil and the calculations were performed using the k-ω model. The time step Δt is non-dimensionalised with the freestream velocity (U_∞) and the aerofoil chord (c).

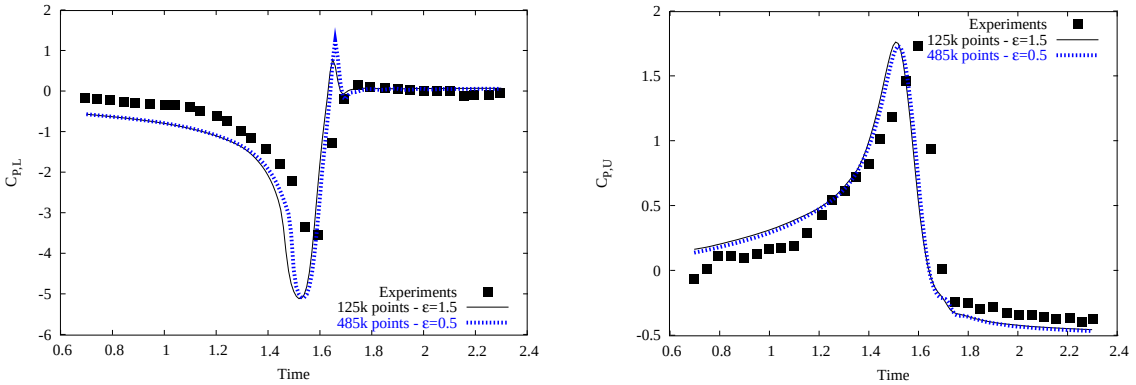

(a) Lower surface, x/c=0.02 (b) Upper surface, x/c=0.02

Figure 8: Influence of the spatial refinement on the time history of the surface pressure coefficient. Head-on BVI problem, NACA-0012 aerofoil, inviscid calculation, Mach number 0.5, x/c=0.02.

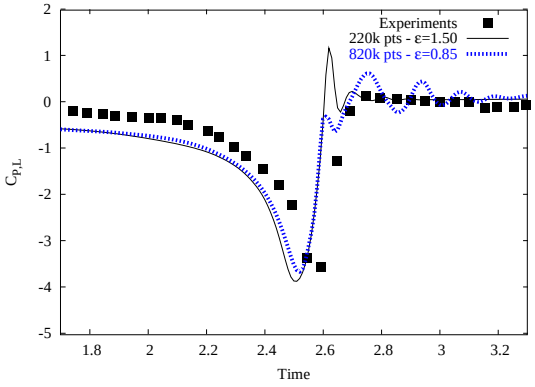

(a) Lower surface, x/c=0.02

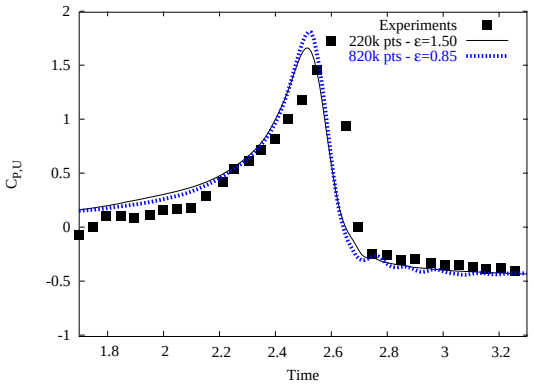

(b) Upper surface, x/c=0.02

Figure 9: Influence of the spatial refinement on the time history of the surface pressure coefficient. Head-on BVI problem, NACA0012 aerofoil, viscous calculation, Mach number 0.5, x/c=0.02.

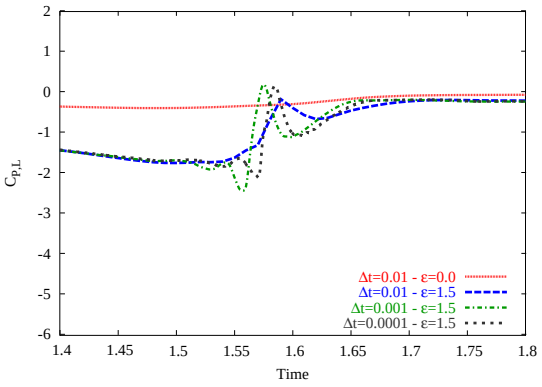

(a) Lower surface, x/c=0.05

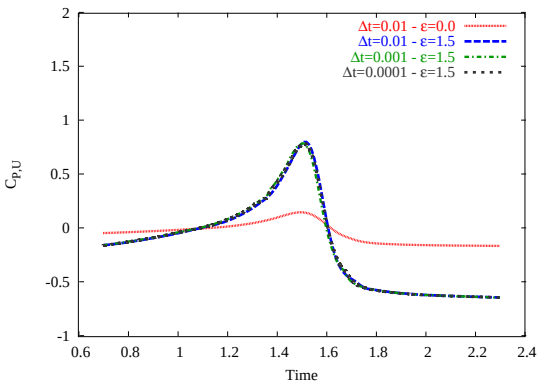

(b) Upper surface, x/c=0.05

Figure 10: Influence of the time refinement on the time history of the surface pressure coefficient. Head-on BVI problem, NACA0012 aerofoil, inviscid calculation, Mach number 0.5, x/c=0.05. The time step Δt is non-dimensionalised with the freestream velocity (U_∞) and the aerofoil chord (c)

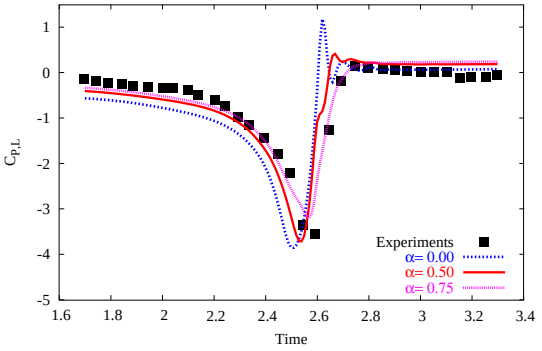

(a) Lower surface, x/c=0.02

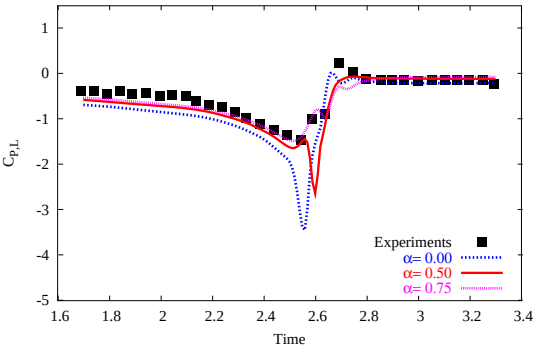

(b) Lower surface, x/c=0.05

Figure 11: Influence of the angle of attack on the time history of the surface pressure coefficient. Head-on BVI problem, NACA0012 aerofoil, viscous calculation, Mach number 0.5. (a) x/c=0.02, (b) x/c=0.05.

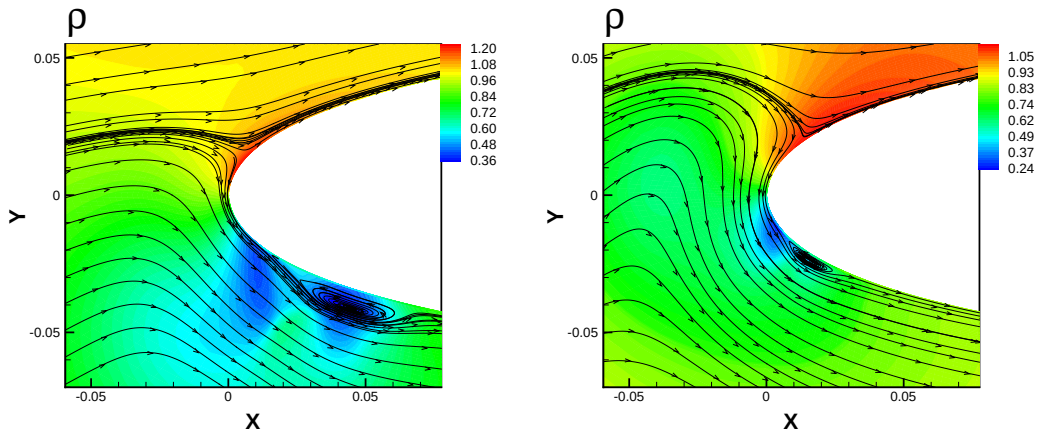

(a) α=0.00 t=2.55 (b) α=0.75 t=2.55

Figure 12: Effect of the angle of attack on the location of the stagnation point. Density contours are shown along with streamlines at the same time instant.

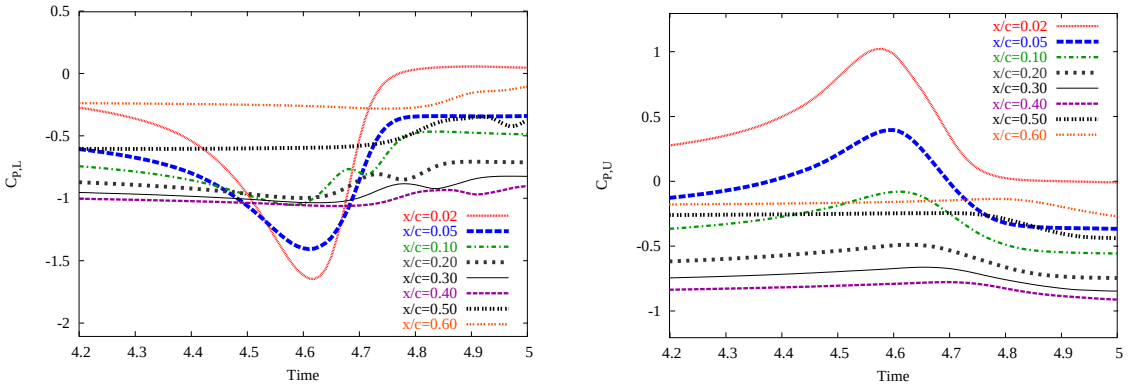

(c) Lower surface (d) Upper surface

Figure 13: Time history of the surface pressure coefficient at different tap locations. Head-on BVI problem, NACA-0012 aerofoil, viscous calculation, Mach number 0.8.

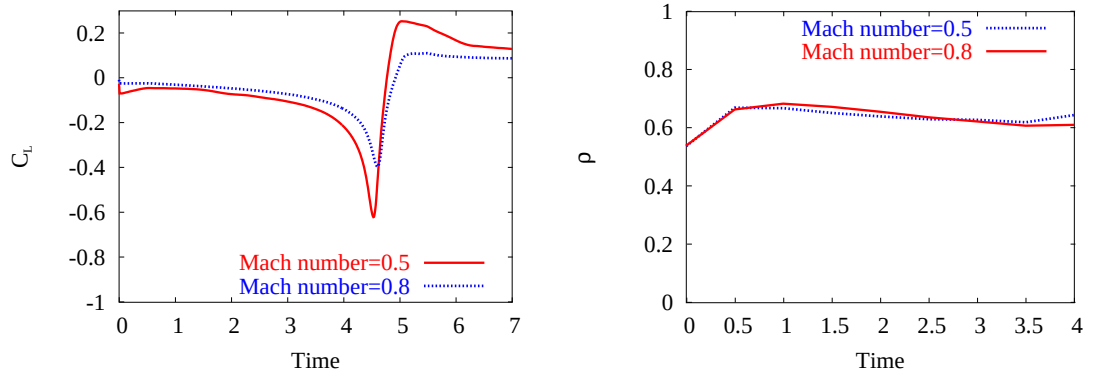

(a) (b)

Figure 14: (a) History of the lift coefficient at Mach numbers of 0.5 and 0.8. (b) Time history of the density at the vortex core at Mach numbers of 0.5 and 0.8.

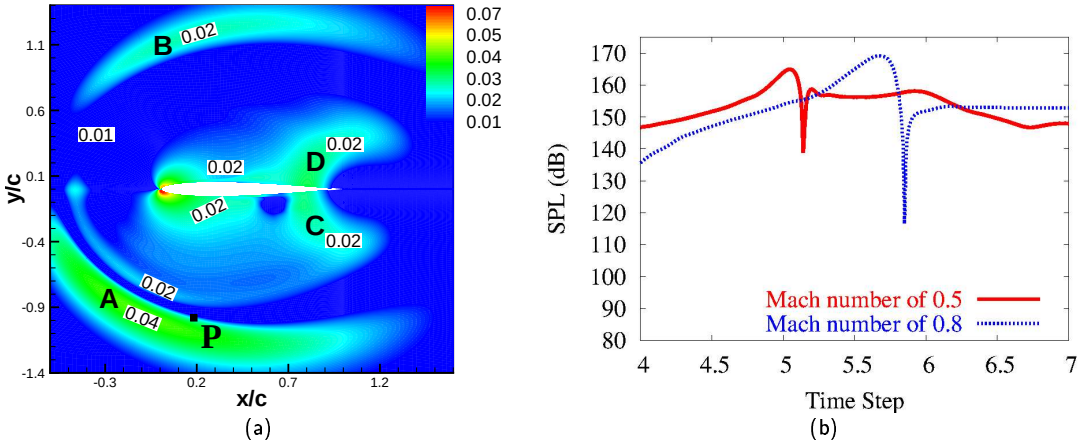

(a) (b)

Figure 15: (a) Absolute value of the acoustical pressure at tU_∞/c=5.01 and Mach number of 0.5. Pressure is non-dimensionalised using the freestream dynamic pressure. (b) Sound Pressure Level history at point P.

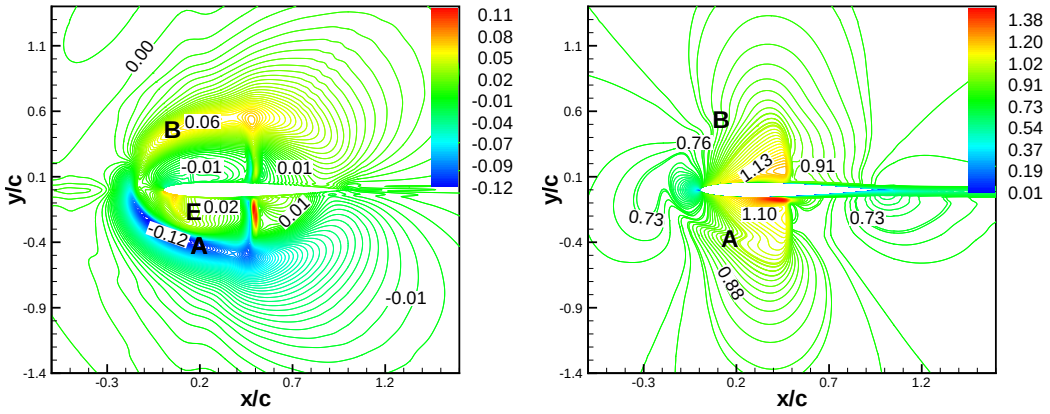

(a) (b)

Figure 16: (a) Acoustical pressure and (b) Mach number contours for the NACA0012 head-on BVI case. The freestream Mach number is 0.8 and (tc/U_∞)=4.95.

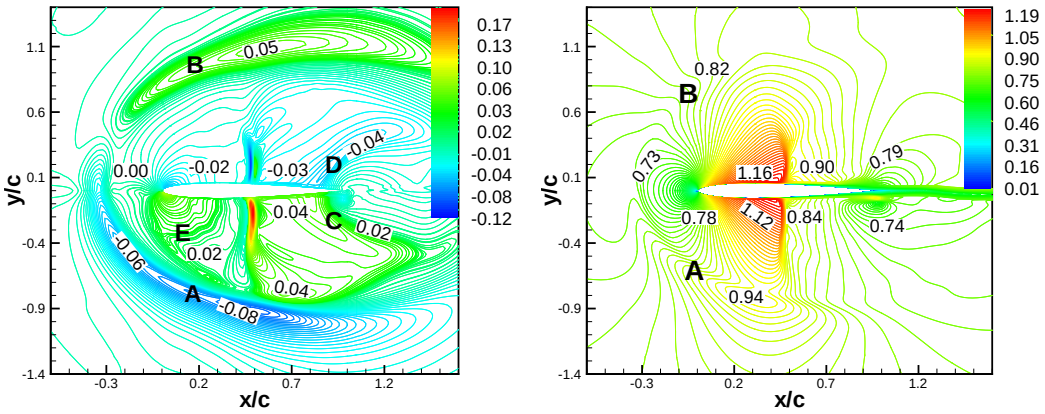

(a) (b)

Figure 17: (a) Acoustical pressure and (b) Mach number contours for the NACA0012 head-on BVI case. The freestream Mach number is 0.8 and (tc/U_∞)=5.40.